J. Fluid Mech. (1992), *vol.* 242, *pp.* 323–347
Printed in Great Britain

Secondary instability in rotating-disk flow

By S. BALACHANDAR[1]†, C. L. STREETT[2] AND M. R. MALIK[1]

[1] High Technology Corporation, PO Box 7262, Hampton, VA 23666, USA

[2] NASA Langley Research Center, Hampton, VA 23665, USA

(Received 7 August 1990 and in revised form 10 February 1992)

Primary instability of the three-dimensional boundary layer on a rotating disk introduces periodic modulation of the mean flow in the form of stationary crossflow vortices. Here we study the stability of this modulated mean flow with respect to secondary disturbances. These secondary disturbances are found to have quite large growth rates compared to primary disturbances. Both fundamental and subharmonic resonance cases are considered and their corresponding results indicate that the growth rate and the frequency of the secondary instability are insensitive to the exact nature of the resonance condition. The threshold primary stationary crossflow vortex amplitude for secondary instability found in this three-dimensional incompressible boundary layer is significantly larger than that for a two-dimensional boundary layer which is subjected to Tollmien–Schlichting instability. The secondary instability results in a pair of travelling counter-rotating vortices, tilted up and oriented at an angle to the primary stationary crossflow vortices. The computed velocity signals and flow visualization, evaluated based on this secondary disturbance structure, are compared with experimental results.

1. Introduction

The laminar-turbulent transition process in three-dimensional boundary layers is of fundamental importance in fluid dynamics, especially in the design of swept wings. However, in comparison with the theoretical and experimental investigations of the transitional flow structures in two-dimensional boundary layers, little is known about the transition phenomenon in three-dimensional flows. In two-dimensional boundary layers the primary Tollmien–Schlichting (TS) instability is followed by pronounced K- (Klebanoff, Tidstrom & Sargent 1962) or C- (Craik 1971) and H-type (Herbert 1984; Kachanov & Levchenko 1984) secondary instability, which then leads to a turbulent regime through a succession of spike stages. Using Floquet theory, Herbert (1984, 1985, 1988) was able to explain the transition process through the secondary instability stage. Further details of the eventual transition process are well documented both by careful experiments and by direct numerical simulations (Kleiser & Laurien 1985; Nishioka, Asai & Iida 1981). In contrast, in a three-dimensional boundary layer only the linear stage of the disturbance growth has been successfully described by the linear stability theory (Gregory, Stuart & Walker 1955; Mack 1984; Malik 1986; Dallmann & Bieler 1987). In this paper we will investigate the secondary stages of the transition process in a three-dimensional rotating-disk boundary layer.

Owing to its simplicity, flow over a rotating disk is often studied to understand the

† Present address: Department of Theoretical and Applied Mechanics, University of Illinois, Urbana, IL 61801, USA.

instability mechanisms present in a three-dimensional boundary layer (Gregory *et al.* 1955; Malik, Wilkinson & Orszag 1981; Kohama 1984, 1987; Kobayashi, Kohama & Takamadate 1980). Unlike the three-dimensional boundary layer on a swept wing, the exact solution to the Navier–Stokes equations for the steady laminar flow (Kármán 1940) on a rotating disk is self-similar and is not complicated by parameters such as pressure gradient and sweep angle. Therefore, the rotating-disk flow is particularly suited to theoretical stability analysis. Moreover, the inflexional crossflow velocity profile, common to both the rotating disk and swept wing, is subject to crossflow instability. Recently Kohama, Saric & Hoos (1991) have performed experiments in a swept-wing boundary layer, where they observe flow structures due to secondary disturbances which are qualitatively similar in nature to those observed by Kohama (1984, and 1987) on a rotating disk. A detailed study of the secondary instability mechanism and the eventual breakdown process in a rotating-disk boundary layer should then improve our understanding of the transition process on a swept wing, when crossflow vortices play the primary role in the transition process.

Wilkinson & Malik's (1983) stability experiments on a rotating-disk flow traced the origin of the primary stationary disturbances, observed in experiments as crossflow vortices, to isolated roughness sites. The wave patterns originating from these roughness sites spread and merge downstream to form approximately thirty vortices whose wave vector is inclined at an angle of about 13° to the radial direction. Mack (1985) used linear theory to simulate the roughness-induced wave pattern and compared the results with those of Wilkinson & Malik (1983). These studies clearly indicated that the stationary crossflow vortices originated at isolated roughness sites. These sites provide streamwise vorticity which is then amplified by the crossflow instability mechanism. Recent experiments performed by W. Saric (private communication) at Arizona State University, on a swept-wing boundary layer, also suggest that the origin of stationary crossflow disturbances is associated with minute roughness sites near the wing leading edge. In his experiment, the transition location moved significantly downstream when the leading-edge region was polished.

In addition to this stationary crossflow disturbance, travelling crossflow disturbances may also be amplified according to linear stability theory. Apart from the inflexional stationary and unsteady crossflow vortices, there are also growing type-II disturbances (Faller 1963; Faller & Kaylor 1966; Mack 1985; Balakumar & Malik 1990) induced by the Coriolis effect. Although the critical Reynolds number for these modes is lower than that for the inflexional modes, the growth rate associated with these type-II modes is small and therefore these modes in general are not expected to play a major role in the overall transition process. In any case, the present investigation is limited to the secondary instability of stationary crossflow.

Flow visualizations on a rotating disk by Kohama (1984) clearly demonstrated the presence of a distinct secondary instability of primary stationary crossflow vortices. Based on the smoke flow pattern, Kohama conjectured that the secondary instability takes the form of ring-like co-rotating vortices appearing on the surface of each stationary primary vortex. His photographs also indicate a strong secondary instability and a rapid transition to turbulence. The presence of secondary instability has also been observed in the hot-wire measurements (Wilkinson & Malik 1983) by the appearance of kinks in otherwise periodic azimuthal velocity signals. Other possible transition scenarios, such as transition through spectral broadening due to nonlinear interaction of two or more primary instabilities cannot be ruled out, although this has not been observed clearly in experiments.

The overall objectives of this paper are to address the following key issues in a three-dimensional rotating-disk boundary layer:

(i) parametric dependence of the secondary disturbance on stationary primary disturbance amplitude, Reynolds number and the resonance condition (fundamental vs. sub-harmonic);

(ii) vortical structure of the secondary disturbance and its relevance to the secondary disturbances observed in flow visualizations;

(iii) qualitative and quantitative nonlinear effects of fine-amplitude primary disturbances on secondary instability.

2. Mean flow and primary disturbance

Consider a three-dimensional boundary-layer flow of an incompressible fluid of density ρ and kinematic viscosity ν on an infinite circular disk rotating at a constant angular velocity Ω. The governing equations for this flow are the Navier–Stokes equations written in a rotating frame of reference:

$$\boldsymbol{u}^*_{t^*} + \boldsymbol{u}^* \cdot \nabla^* \boldsymbol{u}^* = -2\boldsymbol{\Omega} \times \boldsymbol{u}^* - 1/\rho\, \nabla^* p^* + \nu \nabla^{*2} \boldsymbol{u}^* \tag{1}$$

and the incompressibility condition

$$\nabla^* \cdot \boldsymbol{u}^* = 0, \tag{2}$$

where $*$ represents dimensional quantities. An exact solution for the steady laminar mean flow (Kármán 1940) is obtained by setting

$$\begin{aligned} u^* = r^* \Omega u_0(z), \quad v^* = r^* \Omega v_0(z), \\ w^* = (\nu\Omega)^{\frac{1}{2}} w_0(z), \quad p^* = \rho \nu \Omega p_0(z), \end{aligned} \tag{3}$$

where $z = z^*(\Omega/\nu)^{\frac{1}{2}}$ is the non-dimensionalized wall normal coordinate.

For sufficiently large Reynolds number, defined as $R = r_e^* (\Omega/\nu)^{\frac{1}{2}}$ (r_e^* is the radial location where the primary instability analysis is performed), primary instability of the laminar mean flow can occur in the form of crossflow vortices. Defining $r_e^* \Omega$ as the reference velocity, $\delta = (\nu/\Omega)^{\frac{1}{2}}$ as the reference length and $\rho r_e^{*2} \Omega^2$ as the reference pressure, the total instantaneous non-dimensional velocities u, v, w and pressure p can be written as

$$\left.\begin{aligned} u(r,\phi,z,t) &= r/R\, u_0(z) + u_1(z) \exp\left[\mathrm{i}(\alpha_1 r + \beta_1 R\phi - \omega_1 t)\right] + \text{c.c.}, \\ v(r,\phi,z,t) &= r/R\, v_0(z) + v_1(z) \exp\left[\mathrm{i}(\alpha_1 r + \beta_1 R\phi - \omega_1 t)\right] + \text{c.c.}, \\ w(r,\phi,z,t) &= 1/R\, w_0(z) + w_1(z) \exp\left[\mathrm{i}(\alpha_1 r + \beta_1 R\phi - \omega_1 t)\right] + \text{c.c.}, \\ p(r,\phi,z,t) &= 1/R\, p_0(z) + p_1(z) \exp\left[\mathrm{i}(\alpha_1 r + \beta_1 R\phi - \omega_1 t)\right] + \text{c.c.}, \end{aligned}\right\} \tag{4}$$

where c.c. denotes the complex conjugate and $r = r^* (\Omega/\nu)^{\frac{1}{2}}$ is the non-dimensional radius. In the above equation α_1, β_1 and $\omega_1 = (\omega_{1r}, \omega_{1i})$ are the radial wavenumber, azimuthal wavenumber and complex temporal eigenvalue (frequency, growth rate) of the primary disturbance, respectively. Figure 1 shows the local orthogonal coordinates (x, y, z) aligned along the primary vortices in relation to the cylindrical coordinates (r, ϕ, z). The velocity components $\bar{u}, \bar{v}, \bar{w}$ in the vortex-oriented coordinate system, defined as

$$\bar{u} = u\cos\epsilon + v\sin\epsilon, \quad \bar{v} = u\sin\epsilon - v\cos\epsilon, \quad \bar{w} = w, \tag{5}$$

can now be written from (4) as

$$\bar{u}(x,z,t) = r/R\, \bar{u}_0(z) + \bar{u}_1(z) \exp\left[\mathrm{i}(\bar{\alpha}_1 x - \omega_1 t)\right] + \text{c.c.},$$

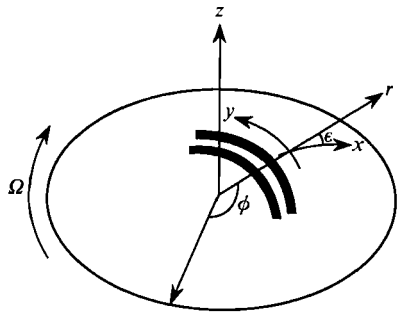

FIGURE 1. Schematic of the rotating disk with the cylindrical (r, ϕ, z) and crossflow (x, y, z) coordinates marked. The crossflow vortices are indicated by the dark patch.

with similar equations for $\bar{v}, \bar{w}$ and p. In (6) the overall primary wavenumber $\overline{\alpha_1}$ and wave angle ϵ are given by

$$\overline{\alpha_1} = (\alpha_1^2 + \beta_1^2)^{\frac{1}{2}}, \quad \epsilon = \arctan(\beta_1/\alpha_1). \tag{7}$$

The appropriate boundary conditions for the primary eigenfunctions are

$$\left.\begin{aligned} &\bar{u}_1(0), \bar{v}_1(0), \bar{w}_1(0) = 0 \\ \text{and} \quad &\bar{u}_1(\infty), \bar{v}_1(\infty), \bar{w}_1(\infty) \to 0. \end{aligned}\right\} \tag{8}$$

Substituting the above equations in the non-dimensional form of the Navier–Stokes equations, an eigenvalue problem for the normal modes can be obtained after linearization. The eigenvalue problem is solved using a Chebyshev collocation method with the physical domain $z \in [0, z_{\max}]$ mapped on to a computational domain $\eta \in [-1, 1]$ by

$$\left.\begin{aligned} &\bar{\eta} = (1-c_1)(\eta^3 - c_2\eta^2 + c^2) + c_1\eta, \\ &z = c_3(1+\bar{\eta})/\left(1 + \frac{2c_3}{z_{\max}} - \bar{\eta}\right), \\ &c_1 = \tan 30°, \quad c_2 = 0.5, \quad c_3 = 1.8, \quad z_{\max} = 20. \end{aligned}\right\} \tag{9}$$

Artificial pressure boundary conditions are avoided by using a staggered mesh in the vertical direction and $N_z = 128$ Gauss–Lobatto (GL) points are used to resolve the computational domain. This results in a generalized eigenvalue problem of the form

$$\boldsymbol{\varphi} = \begin{cases} \boldsymbol{A\varphi} = \omega_1 \boldsymbol{B\varphi}, \\ (\bar{u}_1, \bar{v}_1, \bar{w}_1) & \text{at } N_z \text{ GL points} \\ p_1 & \text{at } (N_z - 1) \text{ Gauss points}, \end{cases} \tag{10}$$

where the matrices $\boldsymbol{A}$ and $\boldsymbol{B}$ are of size $(4N_z - 1) \times (4N_z - 1)$.

Figures 2 and 3 show contour plots of growth rate and frequency of the primary instability in the (α_1, β_1)-plane for $R = 450$. In these figures the radial and azimuthal wavenumbers are normalized by $\alpha_{1s} = 0.328$ and $\beta_{1s} = 0.0699$, wavenumber components corresponding to the most-amplified stationary mode. The overall most-amplified disturbance is a travelling mode with an approximate negative frequency of -7.8Ω, and its radial and azimuthal wavenumbers are approximately α_{1s}, $1.5\boldsymbol{B}_{1s}$. Corresponding contour plots for higher Reynolds numbers are qualitatively similar, but have a larger domain of amplified disturbance. Although the temporal growth

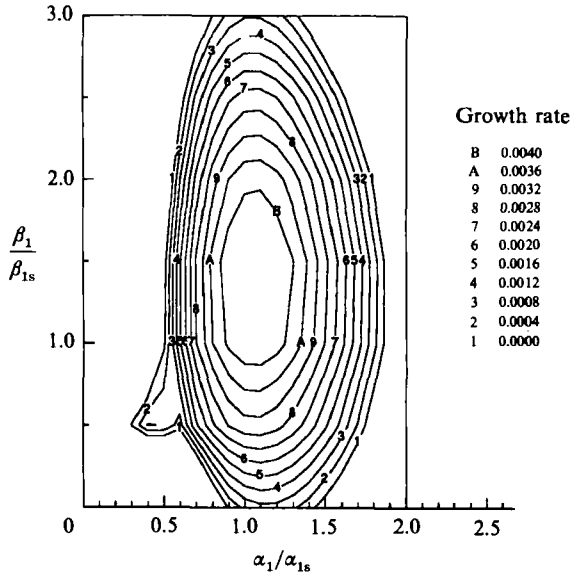

FIGURE 2. Contour plot of primary instability growth rate in the wavenumber (α_1, β_1)-plane for $R = 450$. Here the radial and azimuthal wavenumbers are normalized by $(\alpha_{1s} = 0.328, \beta_{1s} = 0.0699)$, the wavenumber components corresponding to the most-amplified stationary mode. The most-amplified primary disturbance corresponds to a wavenumber of approximately $(\alpha_{1s}, 1.5\beta_{1s})$.

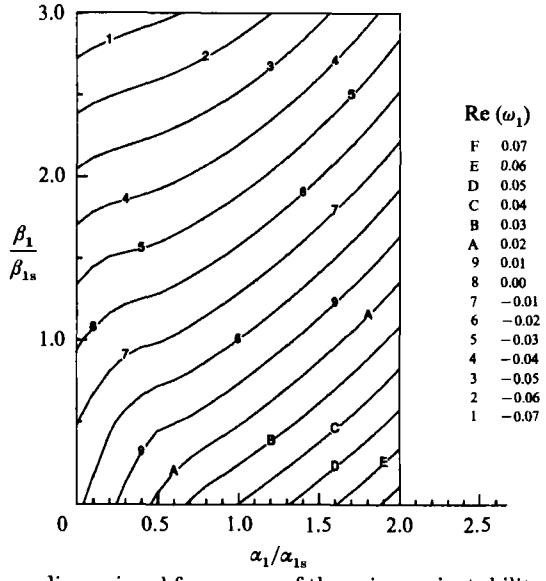

FIGURE 3. Contour plot of non-dimensional frequency of the primary instability in the wavenumber (α_1, β_1)-plane for $R = 450$. Here the radial and azimuthal wavenumbers are normalized by $(\alpha_{1s} = 0.328, \beta_{1s} = 0.0699)$. The most-amplified disturbance is a travelling mode with a negative frequency of -7.8Ω.

rates of the most-amplified stationary and non-stationary disturbances increase with Reynolds number, the wavenumbers corresponding to these most-amplified disturbances remain nearly the same. For further details on the primary instability and its asymptotic structure, the reader is referred to Malik (1986), Balakumar & Malik (1990) and Hall (1986).

3. Secondary instability analysis

The basic state for the secondary instability analysis is given by a finite-amplitude primary disturbance superimposed on the mean flow. This state is periodic both in space (x) and time, and in a frame of reference ($x' = x-(\omega_{1r}/\overline{\alpha_1}\,t)$) moving with the phase speed of the primary disturbance (for a stationary primary disturbance to be considered here this phase speed will be identically zero), the base flow becomes stationary and spatially periodic. The normal mode ansatz for the linear stability of this flow to small three-dimensional disturbances can be performed by writing the total-flow variables in the following form (Herbert 1984, 1985)

$$\bar{u}(x', y, z, t) = r/R\,\bar{u}_0(z) + \epsilon_1\{\bar{u}_1(z)\exp[\mathrm{i}\overline{\alpha_1}x'] + \text{c.c.}\} + \sum_{n=-\infty}^{\infty} \bar{u}_{2n}(z)\exp[\mathrm{i}(n-\sigma)\overline{\alpha_1}x' + \mathrm{i}(\beta_2 y - \omega_2 t)], \quad (11)$$

where β_2 is the secondary wavenumber along the crossflow vortex axis y, and $(\omega_{2r}, \omega_{2i})$ are the frequency and growth rate of the secondary disturbance in the moving coordinate. σ is the detuning parameter; $\sigma = 0$ corresponds to a fundamental secondary disturbance which is periodic over one crossflow wavelength and $\sigma = \frac{1}{2}$ corresponds to a sub-harmonic secondary disturbance which is periodic over two primary crossflow vortices. All other values of σ, $0 < \sigma < \frac{1}{2}$, correspond to combination resonance. In order to define the primary amplitude ϵ_1, we use the following normalization for the primary eigenfunction:

$$\max_{0\leqslant z\leqslant\infty}\left[\frac{\overline{\alpha_1}}{2\pi}\int_0^{2\pi/\overline{\alpha_1}} |v_1(z)\exp(\mathrm{i}\overline{\alpha_1}x) + c.c.|^2\,\mathrm{d}x\right]^{\frac{1}{2}} = \max_{0\leqslant z\leqslant\infty}|v_1(z)| = \frac{1}{\sqrt{2}}, \quad (12)$$

so that ϵ_1 corresponds to the maximum azimuthal root-mean-square fluctuation of the base flow (mean flow + primary) as measured in an experiment.

The use of constant amplitude ϵ_1 in Floquet analysis for the secondary instability is strictly valid only when a nonlinear equilibrium state exists for the primary instability, as in the case of a Poiseuille flow. In order to make the theory applicable to cases where no such equilibrium state exists for the primary disturbance, as in the present case of rotating-disk flow, the following approximations have to be introduced. The first approximation is the quasi-stationary assumption, where the small growth rate of the primary disturbance is neglected in comparison with the relatively strong secondary growth rate. This allows one to ignore the change in the primary amplitude during the short interval of rapid secondary growth. The second approximation is the shape assumption of constructing the base flow by a simple superposition of steady mean flow and a finite-amplitude primary eigenfunction. At large primary amplitudes the effect of nonlinear interaction on mean flow and primary distortion can be significant. Then one needs to include in the analysis these nonlinear distortions, along with the effect of higher harmonics of the primary disturbance, for accurate calculation of the secondary instability. But for small values of ϵ_1, the effect of nonlinearity on this shape assumption is negligible. We will discuss this effect further in §6 below.

Substitution of (11) into the Navier–Stokes equation, along with the boundary conditions

$$\left.\begin{aligned} &\bar{u}_{2n}(0), \bar{v}_{2n}(0), \bar{w}_{2n}(0) = 0 \\ \text{and}\quad &\bar{u}_{2n}(\infty), \bar{v}_{2n}(\infty), \bar{w}_{2n}(\infty) \to 0, \end{aligned}\right\} \quad (13)$$

yields a Floquet system of stability equations with periodic coefficients. As discussed before, depending on the value of the detuning parameter, this system can allow

Modes	n_1, n_2	N_z	z_{max}	ω_2
3	−1,1	33	20.0	0.3874 0.0077
5	−2,2	33	20.0	0.3812 0.0190
7	−3,3	33	20.0	0.3806 0.0221
9	−4,4	33	20.0	0.3805 0.0222
7	−3,3	49	20.0	0.3806 0.0221
7	−3,3	33	40.0	0.3805 0.0223
7	−3,3	49	40.0	0.3806 0.0221

TABLE 1. Effect of Fourier representation and grid resolution

different types of resonance. The resulting equations can be linearized by neglecting nonlinear terms involving secondary eigenfunction, to obtain a linear temporal eigenvalue problem for the complex eigenvalue ω_2. (Note that since the shape assumption ignores nonlinear self-interaction of the primary disturbance, terms of the order ϵ_1^2 are also neglected. Therefore the only quadratic terms retained in the system are the interaction terms between mean flow and secondary, and primary and secondary disturbances.) The eigenvalue problem is solved using a Chebyshev collocation method with the physical domain $z \in [0, z_{max}]$ mapped onto a computational domain $\eta \in [-1, 1]$ by (10), and the solution procedure is the same as that used for the primary instability. As a numerical approximation, the x' dependence of the secondary disturbance in (11) can be represented by a finite Fourier series by replacing the infinite summation by $\sum_{n=n_1}^{n_2}$. Table 1 shows the effect of this truncation in the Fourier representation and the vertical grid resolution on the convergence of the temporal eigenvalue for the fundamental secondary case with

$$\alpha_1 = \alpha_{1s}, \quad \beta_1 = \beta_{1s}, \quad R = 500, \quad \epsilon_1 = 0.12, \quad \beta_2 = 0.65. \tag{14}$$

Based on this table, all further calculations use a seven-mode expansion for the fundamental resonance case with $N_z = 33$ and $z_{max} = 20$. Similarly, a six-mode expansion with $n_1, n_2 = -2, 3$ is used for the sub-harmonic case. A choice of a Dirichlet or asymptotic boundary condition at the finite outer boundary did not alter the overall results.

Table 1 clearly shows that, unlike that for two-dimensional boundary layers, a minimum three-mode Fourier expansion ($n_1, n_2 = -1, 1$) for the fundamental case is not adequate to capture the secondary instability. In order to explain this increase in the resolution requirement, the three components of the velocity eigenfunctions for the seven-mode expansion are shown in figure 4(*a–c*).

The azimuthal velocity eigenfunction corresponding to $n = 1$ is the dominant mode and is normalized to a value of $\sqrt{2}$. With this normalization, the relative amplitudes of the seven azimuthal velocity eigenfunctions ($n_1, n_2 = -3, 3$) are [0.072, 0.150, 0.367, 0.824, 1.414, 1.027, 0.346]. In comparison, the relative amplitudes of the five streamwise velocity eigenfunctions ($n_1, n_2 = -2, 2$) for the Blasius boundary layer are [0.064, 0.848, 1.414, 0.848, 0.064] (Herbert, Bertolotti & Santos 1985). In contrast to the secondary expansion for a two-dimensional TS wave in a two-dimensional boundary layer, the secondary expansion for the rotating-disk case is not symmetric about the dominant harmonic, indicating the absence of a left–right symmetry about the crossflow vortex. For the three-dimensional rotating-disk boundary layer, $n = 0$ is not the dominant harmonic and the convergence of the Fourier expansion is not as rapid. (Of course, by choosing a value of $\sigma = -1$ the most amplified mode can be shifted to the $n = 0$ term of the expansion.)

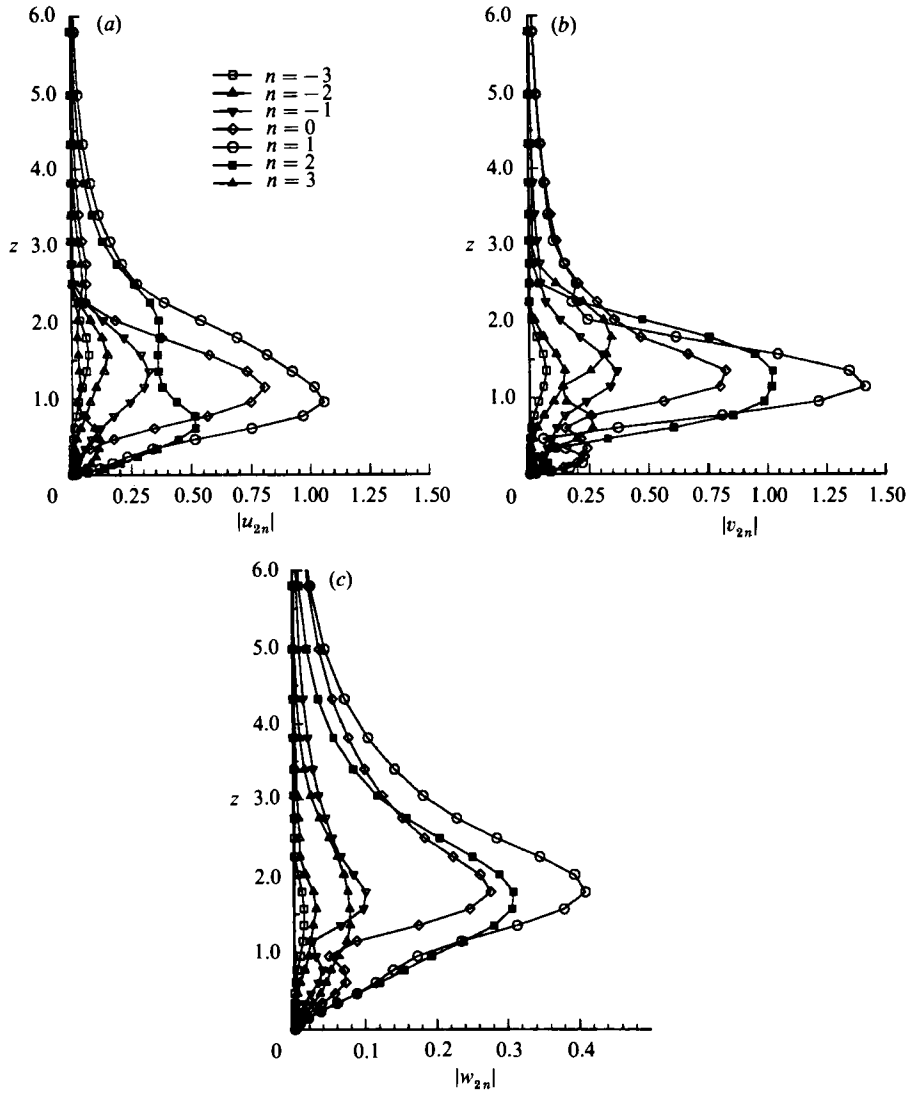

FIGURE 4. Magnitude of the velocity eigenfunctions of the secondary instability for the fundamental resonance case: (*a*) radial component, (*b*) azimuthal component and (*c*) component normal to the disk. A seven-mode expansion ($n = -3, \ldots, 3$), with $Nz = 33$ and $z_{max} = 20$ used in this calculation. The azimuthal velocity eigenfunction corresponding to $n = 1$ is the dominant mode and is normalized to a value of $\sqrt{2}$.

4. Secondary instability results

Let us consider both fundamental and sub-harmonic results corresponding to the most-amplified stationary primary disturbance (α_{1s}, β_{1s}) and let the Reynolds number be 500, unless otherwise stated. Figure 5 shows the fundamental secondary growth rate as a function of the secondary wavenumber along the crossflow vortex (β_2) at a primary amplitude of 12%. For comparison, the primary growth rate is markedly by a dashed line. Although multiple branches of positive growth rate are present, only one branch shows a significantly larger growth rate than the primary. This will be the only branch to be considered for further discussion. A simple estimate based on the experimental photographs of secondary instability (Kohama 1984)

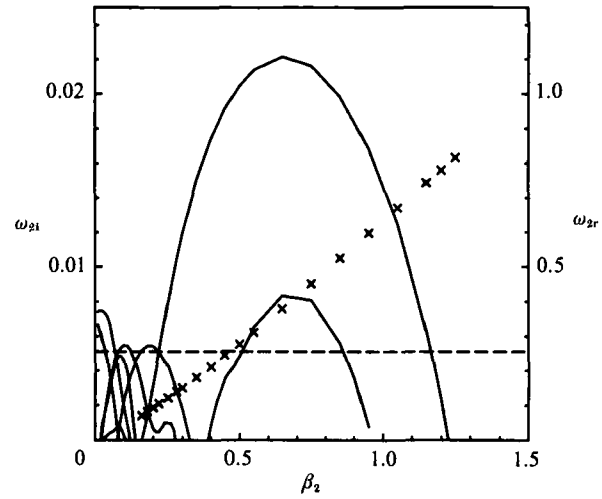

FIGURE 5. Secondary instability growth rate plotted against secondary wavenumber for the fundamental resonance case; $R = 500$, $\alpha_1 = \alpha_{1s}$, $\beta_1 = \beta_{1s}$, and $\epsilon_1 = 12\%$. For comparison, the primary growth rate is marked by a dashed line. Multiple branches of positive growth rate are present, but only one mode shows about four times the primary growth rate. The non-dimensional frequency ω_{2r}, for this fundamental resonance case is represented by $\times$.

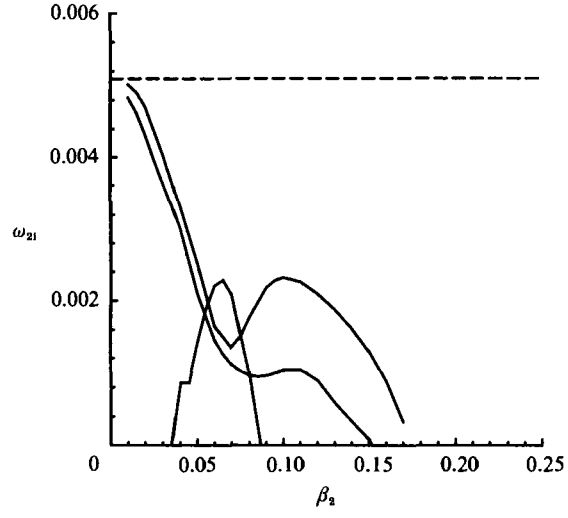

FIGURE 6. Secondary disturbance growth rate plotted against secondary wavenumber for the fundamental resonance case; $R = 500$, $\alpha_1 = \alpha_{1s}$, $\beta_1 = \beta_{1s}$, and $\epsilon_1 = 6\%$. For comparison, the primary growth rate is marked by a dashed line. Multiple branches of positive growth rate are present, but at this lower primary amplitude of 6%, all these branches have smaller growth rate than the primary disturbance.

shows that the secondary disturbance is of fundamental resonance type with a wavenumber β_2 comparable with the computed value of $\beta_2 = 0.65$ corresponding to the maximum secondary growth rate. The secondary instability has growth rate three or more times that of the primary over more than half a decade of wavenumber. The corresponding non-dimensional frequency, ω_{2r} shown in figure 5 as crosses, indicates an almost linear dependence except at small values of secondary wavenumber.

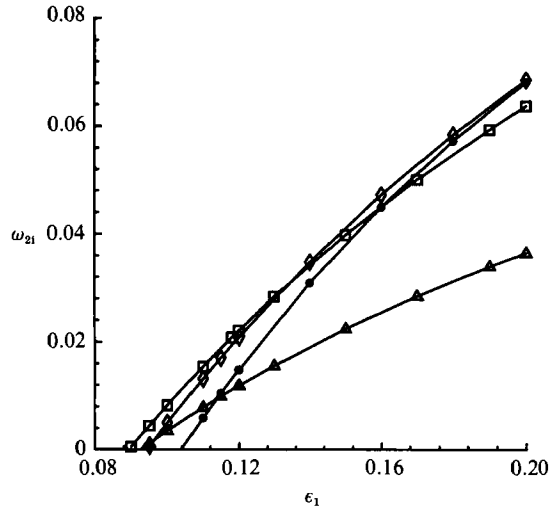

FIGURE 7. Secondary instability growth rate against primary disturbance amplitude for the fundamental resonance case; $R = 500$ and the wavenumber components of the primary disturbance are $(\alpha_{1s}, \beta_{1s})$. Results for four different secondary wavenumbers are presented: △, $\beta_2 = 0.3$; □, $\beta_2 = 0.65$; ◇, $\beta_2 = 0.8$; ●, $\beta_2 = 1.0$. A threshold primary amplitude of approximately 9% is apparent.

A plot of growth rate against secondary wavenumber at 6% primary amplitude (figure 6) shows the absence of the secondary instability at low levels of primary disturbance (some of the other branches with relatively low growth rate are present at this amplitude). This strong dependence of secondary growth rate on primary amplitude is illustrated in figure 7, where ω_{2i} is plotted against ϵ_1 at four different secondary wavenumbers. A threshold primary amplitude of about 9% is apparent, and above this threshold amplitude the secondary growth rate rapidly increases with ϵ_1. According to primary instability theory, disturbances at wavenumbers corresponding to these secondary modes are strongly damped, therefore significant modulation of the steady mean flow by primary disturbance is required. Compared to a threshold amplitude of only a few tenths of a percent needed for secondary instability in two-dimensional boundary-layer flows, a stronger primary disturbance is required for secondary instability in the three-dimensional rotating-disk boundary layer. From figure 7 it can be inferred that as ϵ_1 increases, the secondary wavenumber corresponding to the maximum growth rate also increases. In contrast, figure 8 shows the weak dependence of secondary frequency on primary amplitude.

The effect of Reynolds number on secondary instability is analysed by plotting growth rate against wavenumber for five different values of R at 12% primary amplitude (figure 9). A systematic increase in the maximum growth rate and an associated increase in the wavenumber bandwidth of growing modes is clear. Moreover, since the group velocity of the primary disturbance has a positive radial component, the primary disturbance grows radially and therefore the primary amplitude increases with Reynolds number. This further increases the dependence of secondary growth rate on R. On the other hand, the effect of Reynolds number on the non-dimensional secondary frequency (not shown here) is surprisingly negligible. This in turn indicates a linear dependence of dimensional frequency on Reynolds number, since our earlier choice of length and velocity scales yields a timescale of $1/R\Omega$. For example, for the experimental conditions of Wilkinson & Malik (1983)

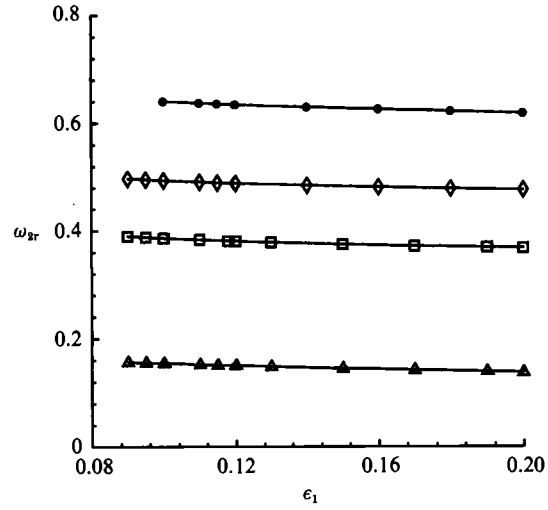

FIGURE 8. The weak dependence of the non-dimensional frequency of the secondary instability on the primary disturbance amplitude for the fundamental resonance case is shown; $R = 500$ and the wavenumber components of the primary disturbance are $(\alpha_{1s}, \beta_{1s})$. Results for four different secondary wavenumbers are presented, symbols as in figure 7.

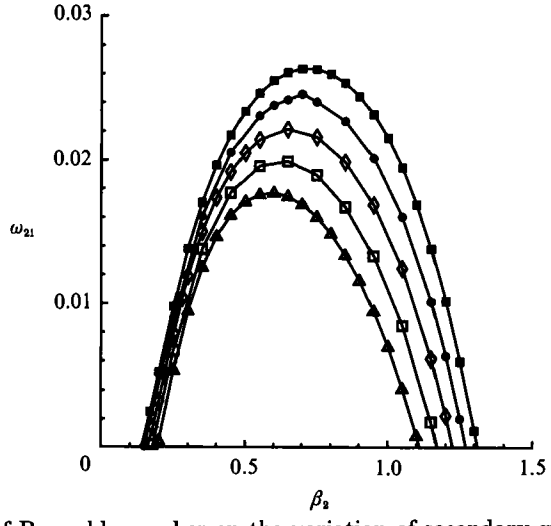

FIGURE 9. Effect of Reynolds number on the variation of secondary growth rate with secondary wavenumber. Primary disturbance amplitude is 12% and the wavenumber components of the primary disturbance are $(\alpha_{1s}, \beta_{1s})$. Results for five different Reynolds numbers are shown: △, $R = 420$; □, $R = 460$; ◇, $R = 500$; ●, $R = 540$; ■, $R = 580$. Maximum growth rate and secondary wavenumber corresponding to the maximum growth rate increase with Reynolds number.

($\Omega \sim 16$ Hz) the dimensional frequency of a secondary disturbance with $\beta_2 = 0.65$ at $R = 500$ will be approximately 3 kHz. The frequency of the secondary disturbance depends upon the flow conditions. Kohama *et al.* (1991) observed the secondary instability spectral peak at 3.5 kHz in their swept-wing experiment. Apparently, a related secondary instability was observed earlier by Poll (1985) in his swept-cylinder experiment. A plot of growth rate against primary amplitude for the five Reynolds numbers with $\beta_2 = 0.65$, figure 10, shows a definite decrease in the

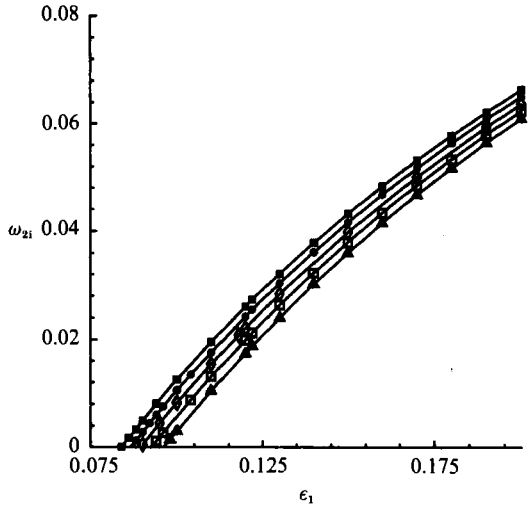

FIGURE 10. Effect of Reynolds number on the variation of secondary growth rate with primary disturbance amplitude. Secondary disturbance wavenumber, $\beta_2 = 0.65$, and the wavenumber components of the primary disturbance are $(\alpha_{1s}, \beta_{1s})$. Results for five different Reynolds numbers are shown, symbols as in figure 9. A definite decrease in the threshold amplitude with increasing R can be observed.

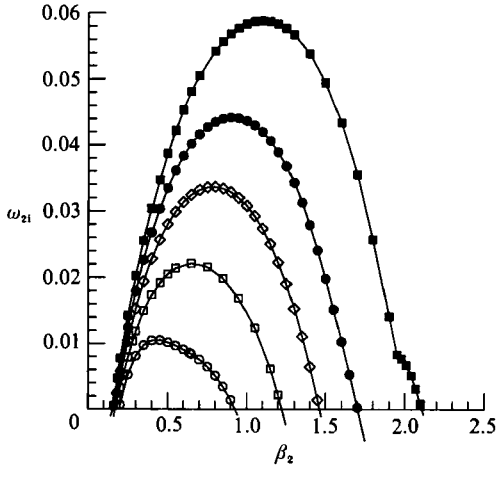

FIGURE 11. Sensitivity of secondary growth rate to changes in the primary instability mode. Growth rate against secondary wavenumber is plotted for five different stationary primary disturbances: ○, $(\alpha_1, \beta_1, \omega_{1i}) = (0.75\alpha_{1s}, 0.83\beta_{1s}, 0.0039)$; □, $(1.0\alpha_{1s}, 1.0\beta_{1s}, 0.0051)$; ◇, $(1.25\alpha_{1s}, 1.20\beta_{1s}, 0.0049)$; ●, $(1.5\alpha_{1s}, 1.41\beta_{1s}, 0.0036)$; ■, $(1.885\alpha_{1s}, 1.8\beta_{1s}, 0.0001)$; $Re = 500$ and the primary disturbance amplitude is 12%.

threshold amplitude with increasing R. For example the threshold amplitude decreases by about 13% for a Reynolds-number increase from 420 to 580. However, we note that transition takes place at a Reynolds number of about 530.

In order to study the sensitivity of secondary instability to changes in the stationary primary disturbance mode, consider figure 11, where fundamental secondary growth rate is plotted against wavenumber for five different stationary primary disturbances $(\alpha_1, \beta_1, \omega_{1i})$ of $(0.75\alpha_{1s}, 0.83\beta_{1s}, 0.0039)$, $(\alpha_{1s}, \beta_{1s}, 0.0051)$, $1.25\alpha_{1s}, 1.20\beta_{1s}, 0.0049)$, $(1.5\alpha_{1s}, 1.41\beta_{1s}, 0.0036)$ and $(1.885\alpha_{1s}, 1.8\beta_{1s}, 0.0001)$ at 12%

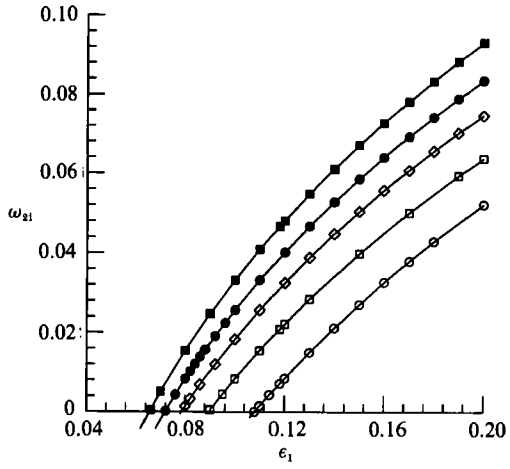

FIGURE 12. Effect of primary disturbance amplitude on secondary disturbance growth rate. Growth rate is plotted for five different stationary primary disturbances: ○, $(\alpha_1, \beta_1, \omega_{1i}) = (0.75\alpha_{1s}, 0.83\beta_{1s}, 0.0039)$; □, $(1.0\alpha_{1s}, 1.0\beta_{1s}, 0.0051)$; ◇, $(1.25\alpha_{1s}, 1.20\beta_{1s}, 0.0049)$; ●, $(1.5\alpha_{1s}, 1.41\beta_{1s}, 0.0036)$; ■, $(1.885\alpha_{1s}, 1.8\beta_{1s}, 0.0001)$; $R = 500$ and the secondary disturbance wavenumber $\beta_2 = 0.65$.

primary amplitude in each case. An increase in both the secondary growth rate and unstable band of wavenumbers is seen with an increase in the wavenumber of the stationary primary disturbance. Moreover, the wavenumber corresponding to the most-amplified secondary disturbance increases; for example the most-amplified stationary primary disturbance ($\alpha_1 = \alpha_{1s}$, $\beta_1 = \beta_{1s}$, $\omega_{1i} = 0.0051$) shows maximum secondary growth at $\beta_2 = 0.65$, whereas the almost neutral stationary primary ($\alpha_1 = 1.885\alpha_{1s}$, $\beta_1 = 1.8\beta_{1s}$, $\omega_{1i} = 0.0001$) shows maximum secondary growth at $\beta_2 = 1.1$.

In figure 12 the effect of primary amplitude on secondary growth rate is considered for a fixed secondary wavenumber $\beta_2 = 0.65$, but for five different primary wavenumbers. A significant decrease in the threshold amplitude can be seen; for example an increase in the primary wavenumber from $(\alpha_{1s}, \beta_{1s})$ to $(1.885\alpha_{1s}, 1.8\beta_{1s})$ decreases the threshold primary amplitude from 9.0% to 6.6%. The threshold amplitudes corresponding to their respective most-amplified secondary wavenumbers are higher than that corresponding to the fixed $\beta_2 = 0.65$ chosen in figure 12. For example for the case of $\alpha_1 = 1.885\alpha_{1s}$, $\beta_1 = 1.8\beta_{1s}$, the threshold amplitude at the most amplified wavenumber $\beta_2 = 1.1$ is 7%, whereas the threshold amplitude at $\beta_2 = 0.65$ is 6.6%. This is because the wavenumber corresponding to the most-amplified secondary disturbance increases as the primary amplitude increases above the threshold amplitude. The threshold amplitudes for the five different stationary primary disturbances considered in figure 12 are therefore close to their corresponding absolute minimum threshold amplitude.

Although primary instabilities with large $\overline{\alpha_1}$ are increasingly susceptible to secondary instability, it should be borne in mind that such small-wavelength stationary crossflow vortices are not the most amplified primary disturbances. Since the threshold amplitude for secondary growth corresponding to the near-neutral primary disturbance ($\alpha_1 = 1.885\alpha_{1s}$, $\beta_1 = 1.8\beta_{1s}$) is significant, it is reasonable to conclude that dominant secondary disturbance is likely to occur only for stationary primary disturbances close to the most-amplitude stationary primary disturbance. Again the effect of primary wavenumber on secondary frequency is negligible.

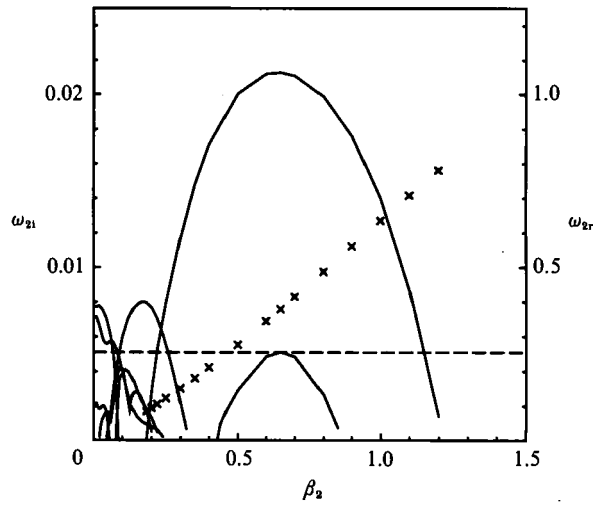

FIGURE 13. Secondary disturbance growth rate plotted against secondary wavenumber for the subharmonic resonance case; $R = 500$, $\alpha_1 = \alpha_{1s}$, $\beta_1 = \beta_{1s}$, and $\epsilon_1 = 12\%$. For comparison, the primary growth rate is marked by a dashed line. Multiple branches of positive growth rate are present, but only one mode shows almost four times the primary growth rate. The non-dimensional frequency, ω_{2r}, for this sub-harmonic resonance case is represented by $\times$.

Figure 13 shows the growth rate of sub-harmonic secondary instability as a function of wavenumber at 12% primary amplitude. Here again multiple branches of positive growth rate can be observed. Except for a very small decrease in the maximum growth rate, the growth rate of the dominant branch is very similar to that for the fundamental secondary case (figure 5). Variations in the secondary growth rate and frequency with primary amplitude and Reynolds number behave in the same way as the fundamental instability. In a two-dimensional boundary layer the threshold primary amplitude for the sub-harmonic resonance was found to be smaller than that for the fundamental resonance (Herbert 1984, 1985, 1988). For the rotating-disk flow the subharmonic threshold amplitude is slightly larger than that for the fundamental resonance. Thus a clear selection mechanism between fundamental and sub-harmonic cases is not present.

5. Comparison with experiments

In order to compare results with experimental flow visualizations and hot-wire measurements, a theoretical flow field can be constructed from (11) with an amplitude ϵ_2 for the secondary velocity. An unambiguous definition for the secondary amplitude results from the following normalization for the secondary eigenfunction:

$$\max_{-\infty \leqslant n \leqslant \infty} \max_{0 \leqslant z \leqslant \infty} |\bar{v}_{2n}(z)| = \frac{1}{\sqrt{2}}. \tag{15}$$

Figure 14(*a*) shows the azimuthal velocity computed in the laboratory frame of reference with $\epsilon_1 = 12\%$ and $\epsilon_2 = 5\%$ for the fundamental resonance case at five different heights from the disk surface. Here the temporal velocity signal is plotted against angle of rotation for comparison with Wilkinson & Malik's (1983) hot-wire measurements. The experimental result was averaged over 50 time records of the

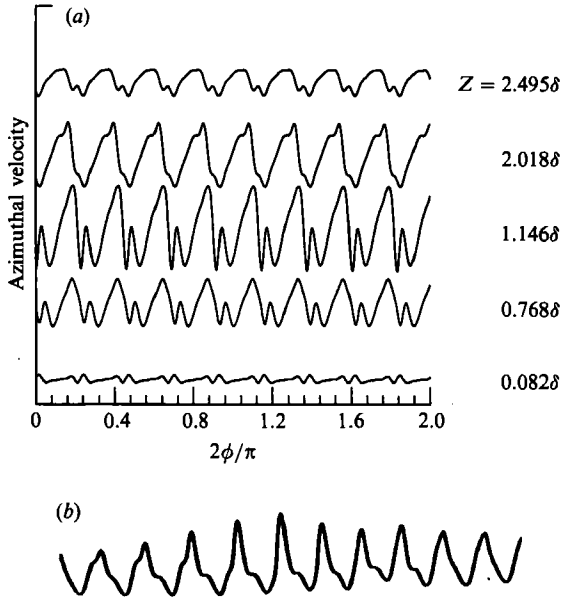

FIGURE 14. (*a*) Computed azimuthal velocity as a function of the angle of rotation at five different heights from the disk. This velocity signal is calculated based on a superposition of the mean flow with 12% primary disturbance amplitude and 5% secondary disturbance amplitude. The primary and secondary disturbances are computed at $R = 500$. The wavenumber components of the primary disturbance are $\alpha_1 = \alpha_{1s}$, $\beta_1 = \beta_{1s}$, and the secondary disturbance wavenumber, $\beta_2 = 0.45$. (*b*) Experimental azimuthal velocity signal (Wilkinson & Malik 1983) measured at $z = 1.9$; R corresponding to the radial location of the experimental measurement is 512.

velocity signal with each record one disk rotation period in length. Therefore to obtain a secondary disturbance, a fundamental secondary disturbance with a wavenumber of $\beta_2 = 0.45$ was chosen in the computation. Comparing the computed velocity signal at $z = 2.018$ with hot-wire trace measured at $z = 1.9$, shown in figure 14(*b*), we can observe that the double-humped kinks observed in the experimental measurements are perhaps due to the secondary instability mechanism.

Further support for the present results comes from a comparison of computed particle traces with the titanium tetrachloride smoke visualizations of Kohama (1984). Particle velocities are calculated based on (11) for the seven-mode fundamental resonance case with $\beta_2 = 0.65$, corresponding to the most-amplified secondary disturbance. A computational flow visualization is performed, in which a total of 2250 marker particles are initially randomly distributed over the horizontal plane $z = 0.35$, well below the core of the primary cortex. The marker particles are first advected in the absence of any secondary disturbance ($\epsilon_1 = 12\%$ and $\epsilon_2 = 0\%$) to capture the effect of the primary disturbance in forming crossflow vortices. The particles are then advected in the presence of 5% secondary amplitude. The resulting snapshot of the particle distribution at a later time is shown in figure 15(*a*). This plot is a plan view from above the disk and it includes two primary wavelengths across the crossflow vortex and three secondary wavelengths along the crossflow vortex ($3\lambda_{ys} = 6\pi/\beta_2$). Here the black background represents the disk surface and the white 'plus' marks indicate the smoke particles. A relatively higher concentration of marker particles can be seen to form vertical patches at the centre and at the two (left and right) edges of this figure. These vertically oriented patches represent the

(a)

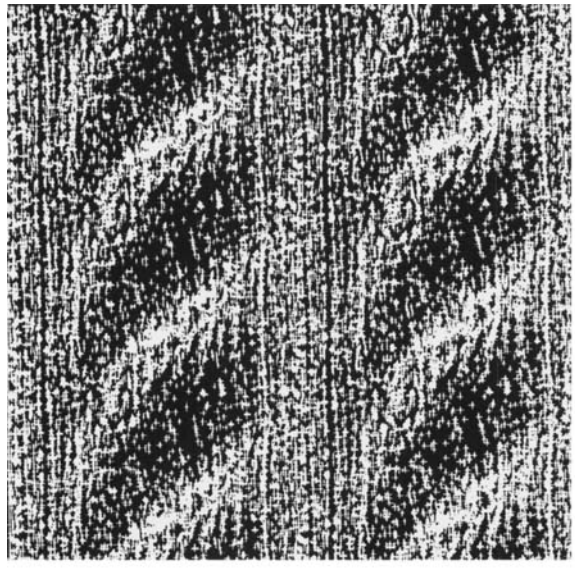

(b)

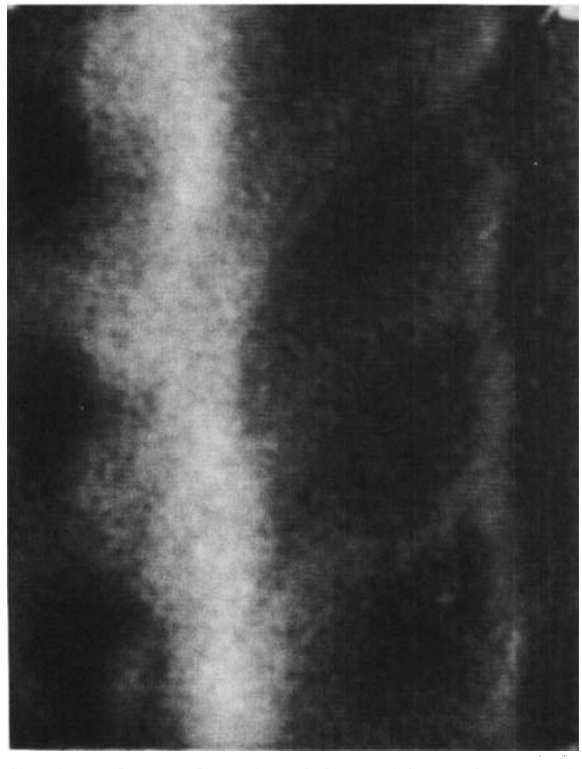

FIGURE 15. (a) Visualization of secondary instability with marker particles advecting in the computed flow field. The visualization is performed with an initial random distribution of 2250 marker particles over a horizontal plane, $z = 0.35$. The marker particles are first advected in a flow field of mean flow plus 12% primary disturbance to capture the formation of the primary crossflow vortices. The particles are then advected in a flow field made up of mean flow, primary disturbance and an additional 5% secondary disturbance. The resulting top view of the marker particle distribution (indicated by white + marks) on a black background is shown. This plot includes two

accumulation of smoke particles in the region below the crossflow vortices due to the action of the primary mode (Kohama *et al.* 1991). The accumulation of marker particles in braids between these vertical patches is due to the secondary instability mode. The corresponding experimental flow visualization photograph of Kohama (1984, 1987)) is shown in figure 15(*b*). Accumulation of smoke below each crossflow vortex can be seen. It is interesting to note that the rib-like structures created by a travelling high-frequency secondary instability observed in the computed results can also be seen in the experimental photograph. It should be emphasized that this comparison is only qualitative owing to the approximations involved in the theory and limitations of the experiment.

Based on the flow visualization, Kohama hypothesized that the effect of secondary instability is to produce helical corotating vortices about the primary vortices. However, such a helical vortex structure is unlikely to be present owing to the proximity of the primary crossflow vortex to the wall. In order to understand the induced flow structure, first consider the effect of primary and secondary disturbances on the overall velocity and vorticity fields. Figure 16 shows the maximum-velocity components across the crossflow vortex (x), along crossflow vortex (y) and normal to the disk for the three cases: (i) mean flow alone, (ii) mean flow + 12% primary and (iii) mean flow + 12% primary + 5% secondary. Here, at each vertical location the maximum velocity is computed in the (x, y)-plane. The corresponding three components of the vorticity distribution are shown in figure 17. Even at low amplitudes, the secondary disturbance significantly increases the velocity components perpendicular to the primary vortex axis. This in turn results in an increase in the vorticity component along the crossflow vortex. The two horizontal components carry more vorticity than the vertical component, but the major contribution to these horizontal vorticities comes from the normal gradients of the horizontal components of velocity ($\partial u/\partial z$ and $\partial v/\partial z$) compared to the horizontal gradients of the normal velocity ($\partial w/\partial x$ and $\partial w/\partial y$).

In order to investigate the secondary vortex structure, we have plotted two-dimensional stream functions for the fundamental resonant secondary velocity field on a number of vertical planes at one time instant. Figure 18(*a–e*) shows contour plots of the stream function in the (x, z)-plane at five different locations along the primary vortex. The y-position of the vertical frame is given in the caption and the stream-function value at the centre of clockwise and anticlockwise rotating vortices corresponding to each position is marked at the top of the frame. At $y = 0$, relatively weak negative vortex can be observed close to the wall near $x = \frac{1}{2}\lambda_p$ and $z = 0.6$. This vortex gains strength and tilts up at an angle as the vertical plane travels down the primary vortex, in other words as y increases. In the final frame, which is half a secondary wavelength away from the first frame, the centre of this negative vortex is at $x = 0.7\lambda_p$ and $z = 1.0$. Owing to the symmetry involved in the secondary expansion the sequence of frames in the second half of the secondary wavelength is the same as in the first half but with the vortices rotating in the opposite sense (frame five is the same as frame one, but for the sign change). Now following the positive vortex, it is clear that the vortex continues to tilt upward, initially continues to gain

primary wavelengths across the cross-flow vortex and three secondary wavelengths along the cross-flow vortex. (*b*) Experimental flow visualization of secondary instability with smoke particles (Kohama 1984, 1987). In the experiment, titanium tetrachloride is coated on a black disk and the smoke pattern resulting from secondary instability is captured in the photograph. This picture includes one primary wavelength across the crossflow vortex and three secondary wavelengths along the crossflow vortex.

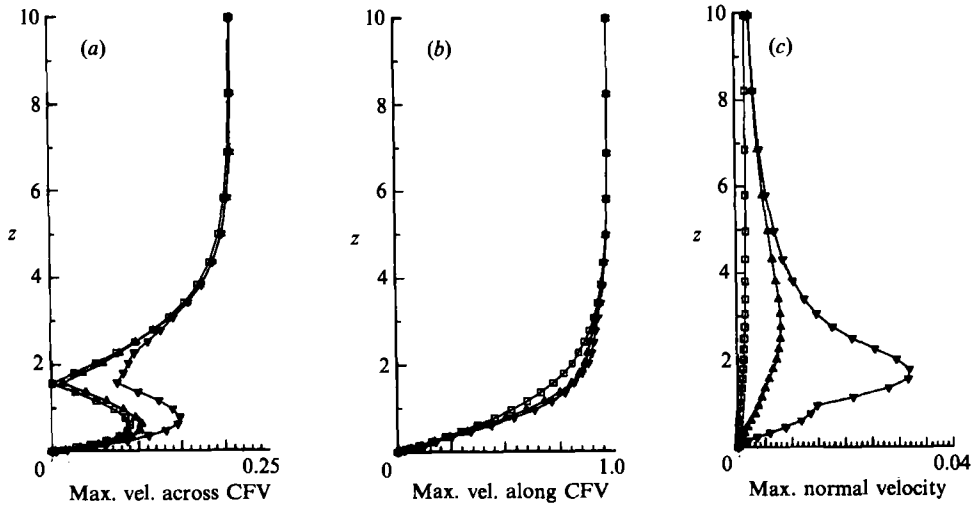

FIGURE 16. Maximum magnitude of the three components of velocity: (*a*) across the crossflow vortex, (*b*) along the crossflow vortex and (*c*) normal to the disk surface. At each z value the maximum velocity magnitude is evaluated over the horizontal (x, y)-plane. Results for the following three cases are presented: □, mean flow only; △, mean flow + 12 % primary disturbance and ▽, mean flow + 12 % primary disturbance + 5 % secondary disturbance.

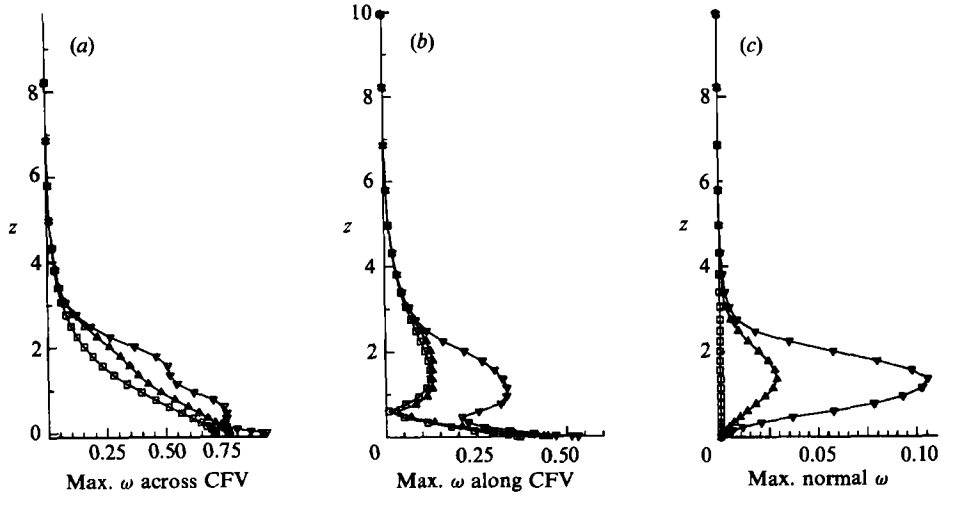

FIGURE 17. As figure 16 but for maximum magnitude of the three components of vorticity.

strength but later weakens away. Thus following the entire length of a secondary vortex it can be seen that the vortex originates around $x = 0.3\lambda_p$ and $z = 0.6$ (see figure 18*c*), extends over one-and-a-half secondary wavelengths along and 0.8 primary wavelengths across the primary vortex, and terminates around $x = 0.1\lambda_p$ and $z = 2.4$ (again see figure 18*c*). Intense regions of the secondary vortex are confined to the right-hand side of the frames; and the maximum intensity occurs at $x = 0.85\lambda_p$ and $z = 1.8$, close to the saddle point of the primary crossflow vortex (see figure 20).

Further evidence for the vortical nature of the secondary disturbance can be obtained from two-dimensional stream-function plots in the (y, z)-plane at a number

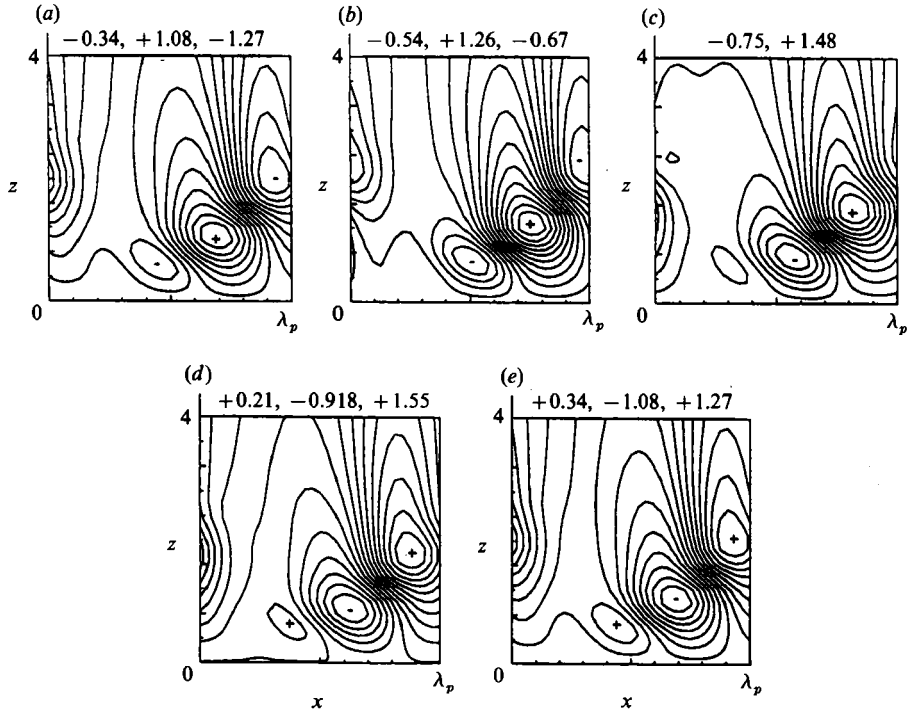

FIGURE 18. Contour plots of the instantaneous stream function of the secondary disturbance in the (x, z)-plane at five different locations along the crossflow vortex. The sign of each vortex is marked in its core and the corresponding stream-function magnitudes are given at the top of each frame. This figure corresponds to a seven-mode fundamental resonance case with a secondary wavenumber of $\beta_2 = 0.65$. (*a*) $y = 0$, (*b*) $y = 0.125\lambda_{ys}$, (*c*) $y = 0.25\lambda_{ys}$, (*d*) $y = 0.375\lambda_{ys}$, (*e*) $y = 0.5\lambda_{ys}$.

of locations across the crossflow vortex. The five frames plotted in figure 19 are for values of $x \geqslant 0.5$. As in figure 18, the stream-function values, or the intensity of the vortices, for $x \leqslant 0.5$ are relatively small and therefore not shown here. The above two figures indicate that the secondary instability results in alternating clockwise and anticlockwise rotating long vortices which are tilted up and oriented at an angle arctan $(1.5\lambda_{ys}/0.8\lambda_p) = 44°$ to the crossflow axis. A schematic of the secondary vortex structure along the primary crossflow vortices is shown in figure 20. It should be noted that when superimposed on the base flow these secondary structures might appear as co-rotating to an observer.

The secondary vortices are centred about the saddle point primary crossflow vortices. These long vortices extend over one-and-a-half secondary wavelengths, but the neighbouring vortices are separated only by half a wavelength. This results in three counter-rotating vortices in any vertical (x, z)-plane along the primary vortex (see figure 18). For this fundamental secondary resonance case, each individual wave in the secondary expansion of (11) travels along its wave vector with phase speed $\omega_{2r}/(\beta_2^2 + n^2\overline{\alpha_1}^2)^{\frac{1}{2}}$. Since each oblique wave travelling at an angle $\theta = \arctan(\beta_2/n\overline{\alpha_1})$ to the crossflow direction has a counterpart travelling at an angle $\theta = \arctan(\beta_2/-n\overline{\alpha_1})$, the combined secondary disturbance travels along the primary vortex axis with phase speed ω_2/β_2. The Lagrangian effect of these travelling tilted counter-rotating vortices is responsible for creating the braids observed in experiments.

Countour plots of the stream function in the (x, z)-plane at different locations along the primary vortex for the sub-harmonic secondary resonance case compare

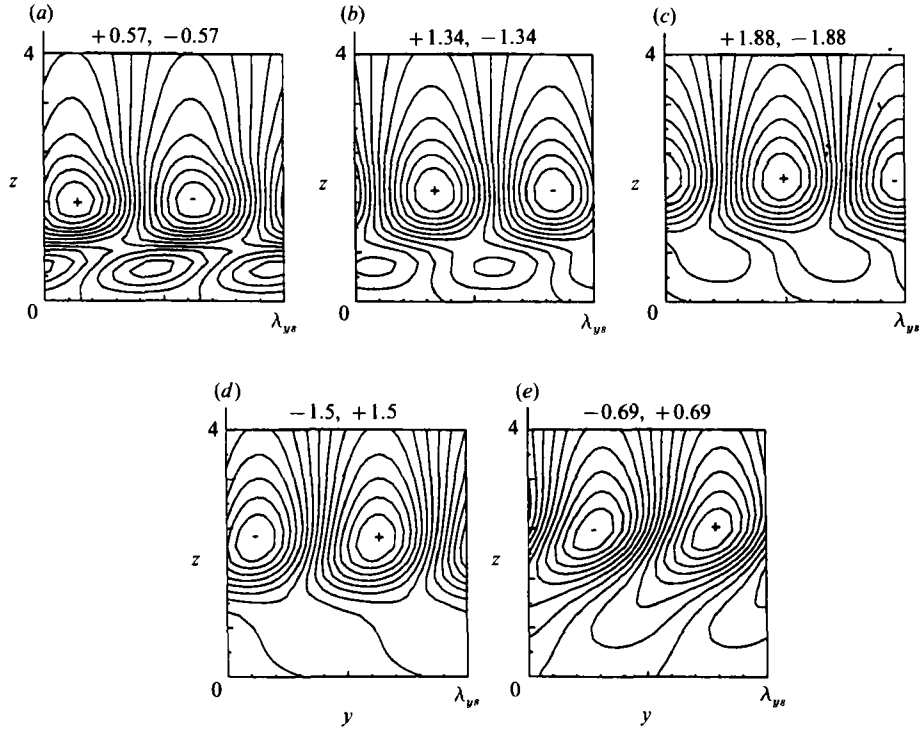

FIGURE 19. As figure 18 but for the secondary disturbance in the (y, z)-plane at five different locations across the crossflow vortex: (*a*) $x = 0.5\lambda_p$, (*b*) $x = 0.625\lambda_p$, (*c*) $x = 0.75\lambda_p$, (*d*) $x = 0.875\lambda_p$, (*e*) $x = 1.0\lambda_p$.

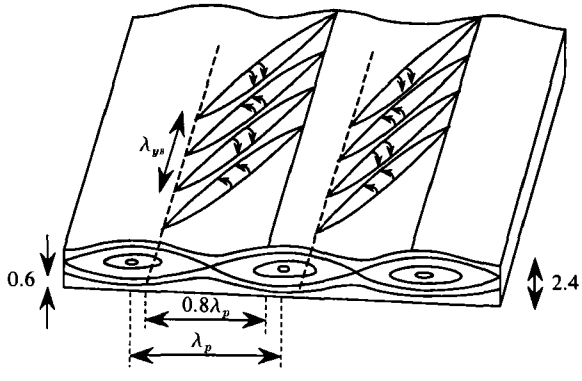

FIGURE 20. Schematic of the vortical structure of the secondary disturbance, superimposed on primary crossflow vortices for the fundamental resonance case. These secondary vortices are counter-rotating and their axes are at an oblique angle to the crossflow vortex axis and are also tilted upwards from $z = 0.6$ to $z = 2.4$. Secondary vortices are centred over the saddle point of the primary crossflow vortices. For this fundamental resonance case adjacent columns of secondary vortices are corotating, whereas in the sub-harmonic resonance case adjacent columns are counter-rotating, and therefore will be shifted by half a wavelength along the crossflow vortex axis.

well with the fundamental resonance case (figure 18), and therefore are not shown here. It appears that the basic structure of the secondary instability is the same in both cases. As before, following the positive and negative vortices from one frame to another it can be inferred that the secondary disturbances are again long upward-

tilting counter-rotating vortices oriented at an angle to the primary crossflow vortex. The difference between the fundamental and sub-harmonic cases lies in the fact that in figure 18 the stream function is periodic over λ_p, whereas in the subharmonic case the stream function is periodic over $2\lambda_p$. The nature of the secondary expansion dictates that the stream function over $\lambda_p \leqslant x \leqslant 2\lambda_p$ is just the same as that over $0 \leqslant x \geqslant \lambda_p$ but with the sign reversed. Owing to this difference, for the fundamental resonance case adjacent secondary vortices sitting on top of saddle points of neighbouring crossflow vortices rotate in the same sense (figure 20), whereas in the subharmonic resonance case they rotate in the opposite sense. Another way to look at this difference is that in the fundamental resonance case adjacent columns of vortices are aligned and in the sub-harmonic case they are shifted by $\frac{1}{2}\lambda_{ys}$ along the primary crossflow vortex. For the combination resonance case this shift will be a non-integer multiple of $\frac{1}{2}\lambda_{ys}$.

6. Effect of nonlinear distortion

Unlike in the two-dimensional boundary layer, the secondary instability in a crossflow-dominated three-dimensional boundary layer occurs only under significant modulation of the mean flow at larger amplitudes of the primary instability. At these primary disturbance amplitudes the shape assumption, which ignores the nonlinear self-interaction of the primary, starts breaking down. In other words, at large values of ϵ_1 the mean flow distortion ($\sim \epsilon_1^2$), primary eigenfunction distortion ($\sim \epsilon_1^3$) and higher harmonics of the primary disturbance ($\sim \epsilon_1^2$) will have a significant influence on the secondary instability (Herbert 1983; Singer, Meyer & Kleiser 1989). If this influence of nonlinearity is solely quantitative, then the secondary instability results based on the shape assumption are relevant to our understanding of the qualitative nature of secondary instability.

In order to assess the effect of nonlinearity, a direct numerical simulation of the nonlinear temporal evolution of the primary crossflow vortex is performed. In the numerical simulation the non-dimensional form of the governing equations (1) and (2) is solved by a spectral method with Fourier expansion in the horizontal directions and Chebyshev expansion, with an algebraic stretching, (9), in the vertical direction. A time-split method (Streett & Hussaini 1990) with a third-order Runge–Kutta scheme for the nonlinear and pressure terms and a Crank–Nicholson scheme for the viscous terms is used. Unlike in Streett & Hussaini, the pressure step is enforced after each state of the Runge–Kutta scheme to reduce the splitting error. The parameters used in this simulation are $R = 500$, $\alpha_{1s} = 0.328068$, $\beta_{1s} = 0.0698504$, which correspond to those used in the secondary stability analysis. Figure 21 shows the evolution of mean flow distortion, total primary amplitude, primary distortion amplitude, and the first and second harmonics of the primary with respect to time. Here the total primary disturbance amplitude is defined as the maximum azimuthal velocity magnitude of the primary eigenfunction. The distortion of the primary disturbance is a measure of the deviation of the computed eigenfunction from the linear eigenfunction. The amplitude and phase of the linear eigenfunction are chosen so that its azimuthal component at its maximum value matches the distorted eigenfunction (Herbert 1983; Singer *et al.* 1989). Significant distortion and nonlinear saturation of the primary crossflow disturbance and its harmonics are evident. For example, when the total primary disturbance reaches a maximum amplitude of about 12.2%, the mean flow distortion is 10.9%, primary distortion is 8.3%, first harmonic is 6.0% and the second harmonic is 3.0%.

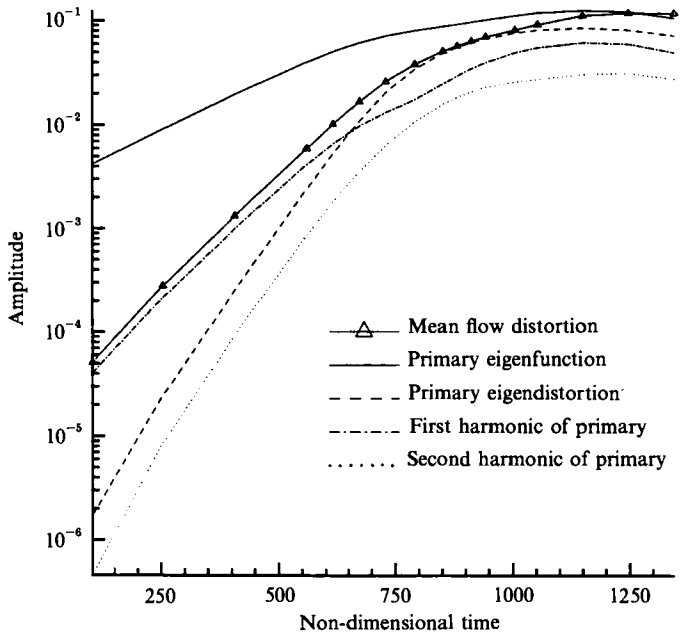

FIGURE 21. Time evolution of mean flow distortion, primary eigenfunction amplitude, primary eigenfunction distortion and amplitudes of first and second harmonics are shown. These results are obtained from a direct numerical simulation of the nonlinear temporal evolution of the primary disturbance in a rotating disk.

At selected instants during the course of the simulation, a base flow consisting of the distorted mean flow and primary eigenfunction along with its harmonics was tested for secondary instability. Multiple branches of positive growth for secondary disturbance were observed. Figure 22 shows a plot of secondary growth rate against wavenumber at four different times for the fundamental resonance case; the corresponding total amplitude of the primary disturbance is also indicated in this figure. Even in the presence of significant nonlinear distortion a broadband secondary disturbance with significant growth rate can be observed. For comparison, the growth rate of the distorted primary crossflow vortex is 0.0021 at $\epsilon_1 = 9.04\,\%$ and 0.0017 at $\epsilon_1 = 10.89\,\%$. These growth rates of the distorted primary disturbance are nearly three times smaller than the undistorted linear primary growth rate of 0.0051. As the primary amplitude increases, the maximum secondary growth rate and the wavenumber corresponding to the maximum growth rate increase. As before, the non-dimensional frequency (not shown here) increases linearly with the wavenumber and shows very little variation with primary amplitude. The wavenumbers corresponding to the maximally amplified secondary disturbances from these base flows are comparable, thus the structure of the disturbance field is similar. The range of wavenumbers, and therefore frequency, over which the secondary growth is significant is also comparable for the distorted and undistorted cases. This qualitative agreement with the earlier results, which were based on the shape assumption, is remarkable considering the potentially significant effect of nonlinearity.

Thus we are lead to believe that the qualitative results for the nature and structure of secondary disturbance obtained with the shape function assumption are valid. Although inclusion of nonlinearity affects the results quantitatively, the overall qualitative picture remains the same. Detailed understanding of the effects of

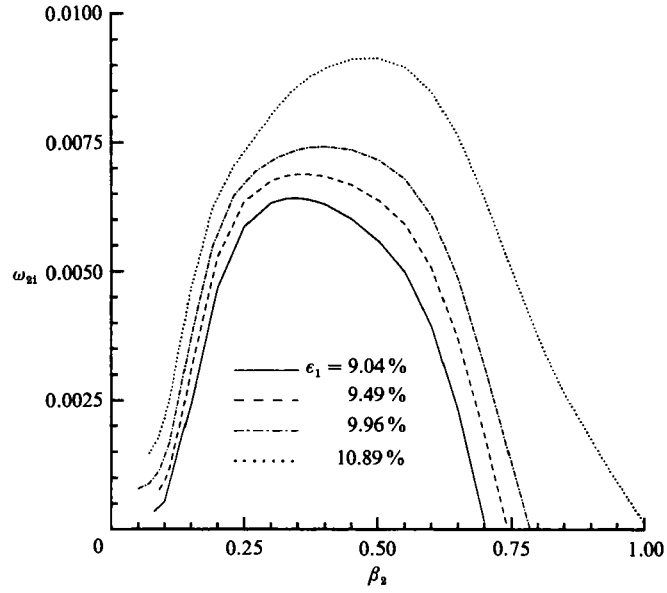

FIGURE 22. Secondary disturbance growth rate plotted against secondary wavenumber at four different amplitudes of primary disturbance. Secondary instability calculations are performed at $R = 500$ and nonlinearly distorted mean flow and primary eigenfunction along with the harmonics are used as the base flow. The wavenumber components of the primary disturbance are $\alpha_1 = \alpha_{1s}$, $\beta_1 = \beta_{1s}$.

nonlinearity needs further study. As a final note, we point out that the relatively large amplitude of the primary instability required for secondary growth is not inconsistent with the experimental data of Wilkinson & Malik (1983) who showed that the crossflow vortices gained large amplitudes prior to breakdown to turbulent motion.

7. Concluding remarks

In two-dimensional boundary layers, Floquet theory of secondary instability has been shown (Herbert 1984, 1985, 1988) to be very effective in explaining the transition process beyond classical linear stability theory. Here this parametric secondary instability analysis has been extended to understand the nature of secondary instability process in a prototype three-dimensional boundary layer on a rotating disk.

In spite of the limitations of the present shape assumption, a number of interesting results can be inferred from the above secondary instability analysis. The underlying structure of the secondary instability is a pair of long counter-rotating travelling vortices tilted upward and inclined at an angle of about 44° to the primary crossflow vortices. Computed results based on this secondary flow structure compare qualitatively with hot-wire measurements and flow visualizations.

An increase in the growth rate and unstable bandwidth of the secondary instability with increasing primary amplitude and Reynolds number has been observed. The secondary frequency shows nearly linear dependence on secondary wavenumber and is also independent of both the primary amplitude and Reynolds number. This indicates an almost constant phase velocity for the secondary disturbance.

Stationary primary crossflow vortices of shorter wavelength were found to be increasingly susceptible to secondary disturbances. On the other hand, such short-wavelength primary disturbances are not the most amplified primary disturbances. A rational approach to the transition problem should include a study of receptivity in order to obtain the initial disturbance spectrum based on global parameters such as surface roughness and free-stream disturbance level. The initial evolution of this disturbance spectrum can then be followed by linear stability theory. When most of the primary disturbance energy is concentrated in a narrow wavenumber band, transition is likely to happen via a distinct secondary instability mechanism. Floquet theory can be used to provide qualitative features of this secondary phenomenon.

The authors are grateful to Drs M. Y. Hussaini, Y. Kohama and A. Kumar for their valuable comments, suggestions and support of this work. The work of S. B. and M. R. M. was funded at National Aeronautical and Space Administration, Langley Research Center under contract number NASI-18240.

REFERENCES

Balakumar, P. & Malik, M. R. 1990 Travelling disturbances in rotating disk flow. *Theo. Comput. Fluid Dyn.* **2**, 125–137.

Craik, A. D. D. 1971 Nonlinear resonant instability in boundary layers. *J. Fluid Mech.* **50**, 393–413.

Dallmann, U. & Bieler, H. 1987 Analysis and simplified prediction of primary instability of three-dimensional boundary-layer flows. AIAA-87–1337.

Faller, A. J. 1963 An experimental study of the instability of the laminar Ekman boundary layer. *J. Fluid Mech.* **15**, 560–576.

Faller, A. J. & Kaylor, R. E. 1966 Investigations of stability and transition in rotating boundary layers. In *Dynamics of Fluids and Plasmas* (ed. S. I. Pai). Academic.

Gregory, N., Stuart, J. T. & Walker, W. S. 1955 On the stability of three-dimensional boundary layers with application to the flow due to a rotating disk. *Phil. Trans. R. Soc. Lond.* A **248**, 155–199.

Hall, P. 1986 An asymptotic investigation of the stationary modes of instability of the boundary layer on a rotating disk. *Proc. R. Soc. Lond.* A **406**, 93–106.

Herbert, T. 1983 On perturbation methods in nonlinear stability theory. *J. Fluid Mech.* **126**, 167–186.

Herbert, T. 1984 Analysis of the sub-harmonic route to transition in boundary layers. AIAA-84–0009.

Herbert, T. 1985 Three-dimensional phenomenon in the transitional flat plate boundary layers. AIAA-85–0489.

Herbert, T. 1988 Secondary instability in boundary layers. *Ann. Rev. Fluid. Mech.* **20**, 487–526.

Herbert, T., Bertolotti, F. P. & Santos, G. R. 1985 Floquet analysis of secondary instability in shear flows. In *Proc. ICASE/NASA Workshop on Stability of Time-dependent and Spatially Varying Flows, Aug. 19–20, Hampton, VA* (ed. D. L. Dwoyer & M. Y. Hussaini). Springer.

Kachanov, Y. S. & Levchenko, V. Y. 1984 The resonant interaction of disturbances at laminar–turbulent transition in a boundary layer. *J. Fluid Mech.* **138**, 209–247.

Kármán, The. von 1940 Uber Laminare und Turbulente Reibung. *Z. Angew. Math. Mech.* **20**, 241–253.

Klebanoff, P. S., Tidstrom, K. D. & Sargent, L. M. 1962 The three-dimensional nature of boundary layer instability. *J. Fluid Mech.* **12**, 1–34.

Kleiser, L. & Laurien, E. 1985 Three-dimensional numerical simulation of laminar–turbulent transition and its control by periodic disturbances. In *Proc. IUTAM Symp. Novosibirsk, 1984* (ed. V. V. Kozlov). Springer.

Kobayashi, R., Kohama, Y. & Takamadate, Ch. 1980 Spiral vortices in boundary layer transition regime on a rotating disk. *Acta Mechanica* **35**, 71–82.

KOHAMA, Y. 1984 Study on boundary layer transition of a rotating disk. *Acta Mechanica* **50**, 193–199.

KOHAMA, Y. 1987 Cross-flow instability in rotating disk boundary layer. AIAA-87–1340.

KOHAMA, Y., SARIC, W. S. & HOOS, J. A. 1991 A high-frequency, secondary instability of crossflow vortices that leads to transition. In *Proc. R. Aeronaut. Soc. Conf. on Boundary-Layer Transition and Control*. Cambridge University.

MACK, L. M. 1984 Boundary-layer linear stability theory. In *AGARD Special Course on Stability and Transition, March 26–30 Rhode-st-Genese, Belgium*.

MACK, L. M. 1985 The wave pattern produced by a point source on a rotating disk. AIAA-85–0490.

MALIK, M. R. 1986 The neutral curve for stationary disturbances in rotating disk flow. *J. Fluid Mech.* **164**, 275–287.

MALIK, M. R., WILKINSON, S. P. & ORSZAG, S. A. 1981 Instability and transition in rotating disk flow. AIAA-81–4225.

NISHIOKA, M., ASAI, M. & IIDA, S. 1981 Wall phenomenon in the final stage of transition to turbulence. In *Transition and Turbulence* (ed. R. E. Meyer), pp. 113–126. Academic.

POLL, D. I. A. 1985 Some observations of the transition process on the windward face of a long yawed cylinder. *J. Fluid Mech.* **150**, 329–356.

SINGER, B. A., MEYER, F. & KLEISER, L. 1989 Nonlinear developments of crossflow vortices. In *Proc. ICASE/NASA Workshop on Stability and Transition, Hampton, VA* (ed. M. Y. Hussaini & R. G. Voigt). Springer.

STREETT, C. L & HUSSAINI, M. Y. 1991 A numerical simulation of the appearance of chaos in finite-length Taylor–Couette flow. *Intl. J. Appl. Numer. Maths Special Issue on Transition to Turbulence* **7**, 41–72.

WILKINSON, S. P. & MALIK, M. R. 1983 Stability experiments in the flow over a rotating disk. AIAA-83–1760